ChemElectroChem

Articles
doi.org/10.1002/celc.202001511

**Chemistry
Europe**
European Chemical
Societies Publishing

Single-Step and Sustainable Fabrication of Ni(OH)₂/Ni Foam Water Splitting Catalysts via Electric Field Assisted Pulsed Laser Ablation in Liquid

Chaudry Sajed Saraj,[a, c] Subhash C. Singh,*[a, b] Abhishek Shukla,[a] Weili Yu,[a]
M. Umer Fayyaz,[d] and Chunlei Guo*[b]

The prevailing barrier to produce hydrogen from water splitting is disappointingly sluggish kinetics. Furthermore, a lack of understanding of the key obstacle in the oxygen evolution reaction (OER), is an obstruction to the design of efficient water-splitting electrocatalysts. Here, we present the single-step and fast fabrication of ready-made Ni(OH)₂/nickel foam (NF) electrocatalysts for overall water splitting by using the environmentally friendly and sustainable approach of electric-field-assisted pulsed laser ablation in liquid for the generation of nanoparticles (NPs) and the simultaneous electrodeposition of the NPs on the NF substrate. The as-fabricated electrocatalyst is found to be highly efficient and stable in alkaline medium for hydrogen evolution reaction (HER) and OER kinetics with

remarkably low overpotentials of 187 mV (vs. RHE for HER) and 166 mV (vs. RHE for OER) to reach a current density of 20 mA cm⁻², with HER and OER Tafel slopes of 82 and 69 mV dec⁻¹, respectively. The two-electrode electrochemical cell made of the bifunctional Ni(OH)₂/NF electrocatalyst requires an overpotential as low as 168 mV to drive a 10 mA/cm² current density over a long period. These results reveal the long-term stability and activity of the Ni(OH)₂)/NF electrocatalyst towards overall water (OW) splitting. The developed sustainable approach of electrocatalyst fabrication can be extended to a range of materials, beyond Ni(OH)₂/NF, to boost a range of chemical reactions, beyond water splitting.

1. Introduction

Supply of energy produced from fossil fuels to fulfil continuously increasing global energy demand has recently surged and given rise to increased greenhouse gases resulting in global warming and associated detrimental effects on climate change.[1–4] The development of carbon-neutral and carbon-negative alternatives to fossil fuel is possibly the most researched area, and has been for several decades.[5,6] Owing to high energy density and carbon free combustion, hydrogen is considered as an ideal and sustainable energy carrier.[7,8] Hydro-

gen production via electrochemical water splitting (EWS) is one of the most efficient and completely green approach.[9–11] However, industrial production of hydrogen through EWS requires cheap, stable and efficient electrocatalysts to boost two half reactions, including hydrogen evolution reaction (HER) and oxygen evolution reaction (OER).[12–14] Among them HER take place at cathode while OER at anode. Unfortunately, these half reactions have different optimal working conditions. HER is generally efficient in acidic environments (i.e. $0.5H_2SO_4$) while OER proceeds effectively in alkaline solutions (such as KOH & NaOH). Due to this issue, water splitting systems need additional accessories to optimize these reactions. Therefore, development of bifunctional electrocatalysts that can facilitate HER and OER in the same electrolyte medium (single cell) is highly desirable for scaled production of hydrogen.

Recently, nickel-based compounds such as NiX (where X: O, S, Se, (OH)₂ and OOH) have attracted intensive attention as an earth-abundant electrocatalyst because of their strong capability to absorb protons on the nickel active sites to make a favorable conditions for the X sites of the structure to bind with reaction intermediates of water splitting.[12–19] In general, catalyst materials are produced using a multistep bottom-up approach that involves hazardous chemicals and toxic biproducts those have adverse impacts on water sources and the environment.[20,21] To minimize the negative impact of hazardous chemical waste on the environment, several green approaches are researched recently to produce nanomaterials, where a chemical precursor is reduced using biological extracts.[22] In spite of multiple rounds of cleaning and centrifugation, chemical residues adsorbed on active sites of

[a]   C. S. Saraj, Dr. S. C. Singh, Dr. A. Shukla, Dr. W. Yu
     GPL, Changchun Institute of Optics
     Fine Mechanics and Physics
     Chinese Academy of Sciences
     Changchun 130033, China
     E-mail: ssingh49@ur.rocheester.edu
[b] Dr. S. C. Singh, Prof. C. Guo
     The Institute of Optics
     University of Rochester
     Rochester, NY 14627, USA
     E-mail: ssingh49@ur.rocheester.edu
            guo@optics.rochester.edu
[c]   C. S. Saraj
     University of Chinese Academy of Sciences (UCAS)
     Beijing 100049, China
     E-mail: sajedsaraj@ciomp.ac.cn
[d] M. U. Fayyaz
     Key laboratory of Advanced Materials (MOE)
     School of Materials Science and Engineering
     Tsinghua University
     Beijing, 100084, China

ChemElectroChem

Articles
doi.org/10.1002/celc.202001511

Chemistry Europe
European Chemical
Societies Publishing

electrocatalysts limits their electrochemical surface area (ESCA) and hence water splitting performance.

Recently, applications of lasers have been dramatically extended from conventional cutting and drilling to advanced material nanopatterning and surface functionalization. Selective thinning of two-dimensional MoS_2 flakes,[23] patterning of thin graphene for optoelectronics applications,[24] and surface texturing to alter optical and wetting properties[25,26] are only a few examples. These surface processing techniques enable regular material to exhibit unmatched functionalities and surprising applications. For example, in a recent work, femtosecond laser processed black and super-wicking metal surface was used to fabricated highly efficient solar-thermal water purification device.[27] Among these, laser ablation in liquids (LAL) is a rapid, versatile, environment friendly, entirely physical top-down, and sustainable approach to produce colloidal solution of nanoparticles (NPs) for a range of applications.[28–30] Unlike chemical approaches, the NPs produced through LAL has surfaces free from any chemical residues thus they have excellent catalytic performance.[31–34] Moreover, the LAL produced NPs have a surface charge that provides colloidal stability in the solution through Coulombic repulsion. Although, LAL has several advantages in the synthesis of NPs, but applications of these NPs are limited to solution phase. For example: Electrocatalytic applications of these NPs generally require their separation from the solution through centrifugation, dispersion in the alcohol and Nafion mixture, and redeposition on a glassy carbon electrode for electrochemical measurements.[31]

These multistep, multi-pot, complex, and time consuming processes increases overall fabrication time of electrocatalyst, thus limits their electrocatalytic applications in industrial scale hydrogen generation.

Herein, we present a single-step-single-pot synthesis of Ni $(OH)_2$ spherical NPs via electric field assisted pulsed laser ablation (EF-PLAL) of Ni in DI water and simultaneous di-electrophoretic deposition of as-produced NPs on nickel foam (NF) to fabricate readymade $Ni(OH)_2$/NF electrocatalysts on support for overall water splitting. The laser pulse energy of 0.5 mJ/pulse is used to ablate the material, and electric field is controlled by a variable DC supply, The $Ni(OH)_2$/NF electrocatalysts are synthesized at different applied electric fields (1, 5, 10, 25, and 40 V/cm) and named as $Ni(OH)_2$/NF@E_field. By this way we prepared five electrocatalysts as $Ni(OH)_2$/NF@1 V, Ni $(OH)_2$/NF@5 V, $Ni(OH)_2$/NF@10 V, $Ni(OH)_2$/NF@25 V, and $Ni(OH)_2$/ NF@40 V. The developed method is ultrafast, simple, sustainable, environment-friendly, and does not require any post processing step like deposition/coating/loading and adhesive. The fabricated electrocatalysts show superior HER/OER activity with excellent durability. The $Ni(OH)_2$/NF@40 V electrode is the most efficient, among all, for both electrocatalytic HER and OER activities. Importantly, when two $Ni(OH)_2$/NF@40 V electrocatalyst sheets, one as a cathode and second as an anode, are assembled in a two-electrode cell, it requires only 1.68 V of potential to drive 10 mA/cm² of current density with an excellent stability even after 20 hours of operation. This work opens a horizon in designing of high-efficiency ready-to-use catalyst sheets, for a wide range, beyond HER and OER, of chemical reactions.
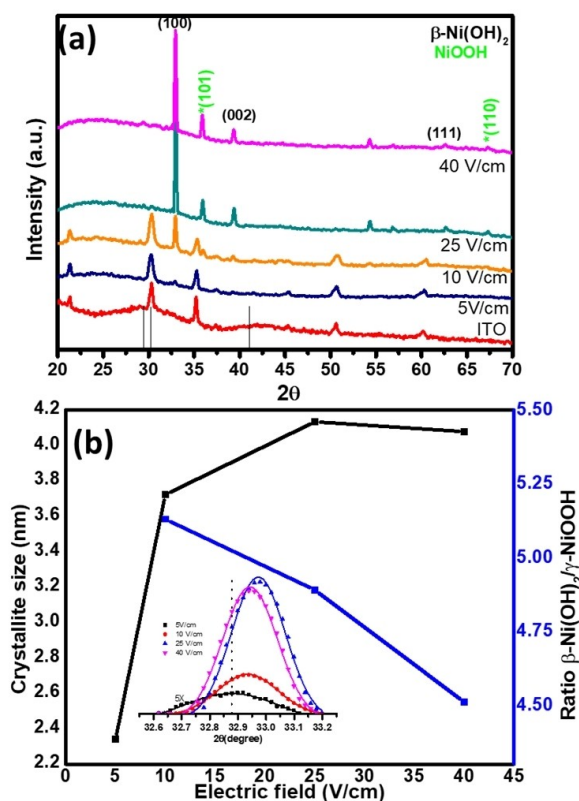
2. Results and Discussion

The fabrication process of $Ni(OH)_2$/NF electrocatalysts is shown in Scheme 1. A Ni disc, placed at the bottom of a glass vessel with 1 cm thickness of distilled water overlayer, was ablated at solid-liquid interface to produce $Ni(OH)_2$ NPs in the solution. Two Ni Foam (NF) electrodes, separated by 1 cm, were mounted across the laser produced plasma (LPP) plume, the nucleation and growth region of NPs, to electrophoretically deposit as produced $Ni(OH)_2$ NPs on the electrodes to fabricate ready-to-use electrocatalysts on the support (Supporting Information Figure S1). The intensity of applied electric field controls size, morphology, and density of $Ni(OH)_2$ NPs in the $Ni(OH)_2$/NF electrocatalysts.

2.1. Structural, Compositional and Morphological Characterization of EF-PLA-Produced Electrocatalysts

In order to determine the structural phase of EF-PLA produced NPs using X-ray diffraction we used ITO coated glass electrodes, instead of Ni foam, for application of E-field and electrophoretic deposition of NPs $Ni(OH)_2$ to avoid a confusion that XRD peak is from the NPs or from the Ni foam substrate. The X-ray diffraction patterns of NPs produced at different applied electric fields are shown in Figure 1 (a). The samples produced via EF-PLA under higher electric fields (25 and 40 V/cm) have a strong, while those produced at lower electric fields (5 and 10 V/cm) have comparatively weaker diffraction peaks at $2\theta = \sim 32.8°$ corresponding to the Bragg reflection of (100) plane of β-Ni $(OH)_2$. The weaker diffraction peaks are assigned to (002) and (111) diffraction peaks of β-$Ni(OH)_2$ and (101) and (110) diffraction peaks of γ-NiOOH (JCPDS 6-0075). The (100) peak of
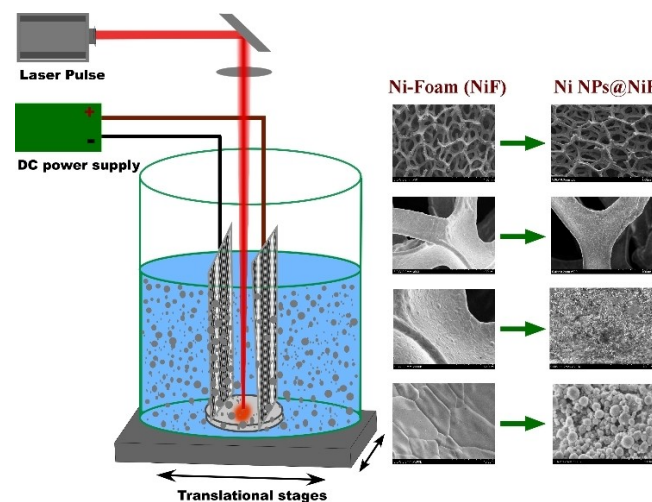
**Scheme 1.** Schematic illustration of the synthesis and structure of $Ni(OH)_2$ nanospheres on Ni foam.

ChemElectroChem

Articles
doi.org/10.1002/celc.202001511

**Chemistry
Europe**
European Chemical
Societies Publishing

Figure 1. Structural characterization of Ni(OH)$_2$NPs: a) XRD spectra of EF-PLA-produced NPs under different applied electric fields. b) Variation in the particle size (black line) and areal intensity of (100) peak of β-Ni(OH)$_2$ EF-PLA produced and deposited at ITO-coated glass substrate at different electric fields. Inset: Gaussian fitting of (100) peak to determine particle size and relative intensity. The (100) peak is magnified five times for visualization.

β-Ni(OH)$_2$ NPs is used to estimate their crystallite size using the Scherrer's formula. The crystallite size of the NPs increases with increase in the applied electric field in the range of 5 to 25 V/cm range and decreases slightly at a higher electric field (Figure. 1(b)).

The areal intensity of XRD peaks can be used for a quantitative estimation of the density of NPs deposited on the electrodes at a given applied electric field and degree of crystallinity of NPs. An increase in the areal intensity of the (100) diffraction peak with the applied electric field shows that the rate of deposition of NPs increases linearly with E-field in the range of 5 to 25 V/cm (supporting information Figure S2). The decrease in the optical transmission of NPs, deposited on ITO coated glass substrate, with increase in the applied electric field also shows an increase in the density of NPs on the substrate with the applied electric field (supporting information Figure S3). A slight decrease in the areal intensity of (100) peak for NPs produced at 40 V/cm field (Figure 1a), where the density of NPs is higher, is possibly result of decrease in the crystallinity due to formation of defects. Slight decrease in the areal intensity of (100) diffraction peak for 40 V/cm of applied E-filed as compared to 25 V/cm is possibly due to the same reason.

The ratio of (100) diffraction peak of β-Ni(OH)$_2$ with (101) diffraction peak of γ-NiOOH can be used to determine their

relative population densities. Increase in the applied electric field decreases the value of β-Ni(OH)$_2$/γ-NiOOH (Figure 1(b), blue line). These investigations show that the ratios of β-Ni(OH)$_2$ and γ-NiOOH in ready-to-use electrocatalysts lie in the range of ~5.1 to 4.5. To determine the surface composition of as-prepared Ni(OH)$_2$/NF electrocatalysts, X-ray photo-electron spectroscopy (XPS) measurements were carried out (supplementary Figure S4). Generally, the oxidation state of Ni at the surface can be derived from the binding energies and their chemical shifts in the XPS.[35] The magnified spectrum for Ni 2p and O 1s region was exhibited in Figure 2 (left column & right column respectively). The Ni 2p spectrum is deconvoluted into two spin orbit doublets at 852.5 eV, 854.0 eV and 855.73 eV corresponding to metallic Ni, γ-NiOOH and Ni(OH)$_2$, respectively. The XPS peaks at 854.0 and 855.73 eVs are assigned to Ni^{3+} and Ni^{2+} species, respectively. The satellite peaks of Ni 2p located at 861.2 eV and 879.2 eV.[34] For the as-prepared samples, the peak at a binding energy of 855.73 eV, corresponding to Ni 2p3/2 with the satellite at 861.5 eV, indicates presence of Ni(OH)$_2$[31] (as shown in Figure 2 left column). The peak at binding energy 854.5 eV corresponds to Ni^{+3} oxidation state of NiOOH. From the XPS measurements, we can also see that the population of NiOOH increases with increase in the applied electric field, consistent with the XRD measurements. It can be seen from Figure 2 (right column) that the O 1s spectrum at 531.3 eV is
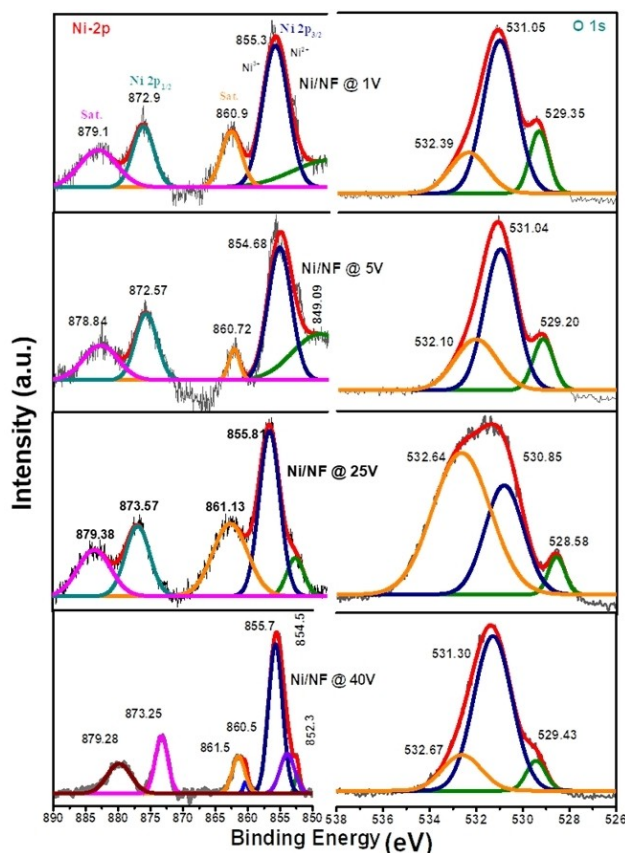
Figure 2. XPS spectra of Ni@NPs produced under different bias voltages 1 V, 5 V and 25 V (bottom), 40 V (top) of applied electric fields: a, b) Ni 2p and c, d) O 1s peaks.

ChemElectroChem

Articles
doi.org/10.1002/celc.202001511

Chemistry Europe
European Chemical
Societies Publishing

also consistent with Ni(OH)$_2$ formation. The scanning electron microscopy (SEM) were used to explore surface morphologies of as-prepared Ni(OH)$_2$/NF electrocatalysts. Figure 3 and supplementary Figure S5 show the scanning electron microscopy (SEM) images of different EF-PLA fabricated Ni(OH)$_2$/NF electrocatalysts.

At lower electric fields (1 and 5 V/cm), football shaped NPs in the size range of 20–100 nm are formed. Since the density of NPs on the Ni foam substrate is low, we can see individual NPs and Ni foam substrate. The corresponding transmission electron microscopy (TEM) images, presented in Figure S6 (a,b), show presence of NPs in the size ranges of 5–45 nm and 1–13 nm in the solutions produced under 1 and 5 V/cm of applied electric fields, respectively. At a medium electric field (10 and 25 V/cm), NPs with bimodal size distributions are formed. Ultrafine NPs with size < 10 nm are in abundance ($> 95\%$ of populations) with formation of few ($< 5\%$) larger sized (20–80 nm) spherical NPs. Increase in the electric field causes increase in the density of ultrafine NPs while decreases in the density of larger sized spherical balls (Supplementary Figure S5). The corresponding TEM image (Figure S6 (c)) also shows a significant decrease in the population of larger (> 10 nm) size NPs at higher (10 V/cm) applied electric field.

The lower resolution (left panel of Figure 3) of these SEM images shows a layer-by-layer deposition of NPs on the Ni foam with a comparatively higher rate of deposition at the edges due to comparatively stronger electric fields (*see* the second column of Supplementary Figure S6). The nanostructured films formed from the NPs produced and deposited at the higher applied E-field (left panel Figure 3a *versus* 3c)) has comparatively lesser

cracks and higher packing density due to high density of ultrafine NPs (right panel Figure 3a *versus* 3c). The average size of NPs produced and deposited at Ni foam under lower electric (1, and 5 V/cm) are ~ 79 nm, and 70 nm. The average size of ultrafine NPs produced at 40 V/cm of applied field is 4 ± 0.5 nm (Supporting Information Figure S6). The corresponding TEM image, shown in Figure S6(d), also shows presence of ultrafine (< 7nm) NPs in the solution. The compositional ratios of Ni and O in the Ni(OH)$_2$/NF electrocatalyst samples, as obtained by EDS spectra (*see* Table 1 and Table 2), are close to the compositional results obtained from the XPS measurements.

From SEM and TEM investigations, we can see that the size of NPs produced in the solution or electrophoretically deposited on NF electrodes decreases with increase in the applied electric field. To understand the reason behind, it is important to understand the supply of precursors (Ni and OH ions) through laser ablation of Ni target and thermal dissociation of water molecules at plasma-water interface, and growth, stabilization, and transport of NPs[29] Laser ablation of Ni target at target-water interface generates high temperature, high density, and high pressure (HTHDHP) plasma, known as laser, produced plasmas (LPPs), confined under water overlayer. The LPPs, containing Ni ions, reacts with surrounding water molecules at the plasma-water interface to ionize them and generates plasma-induced-plasmas (PIPs) containing constituents (H$^+$ and OH$^-$) of water .[24] The Ni ions from LPPs reacts with the OH$^-$ ions from PIPs at LPPs-PIPs interfaces to generate nuclei of Ni(OH)$_2$ NPs. The H$^+$ ions from the PIPs possibly get deposit on the surface of Ni(OH)$_2$ NPs to generate a positive surface charge. The rate of growth of the NPs and generation of new nuclei in the growth region depend on the concentration of cationic and anionic species and local temperature. At a given rate of growth of NPs, size of the final NPs depends on the time they spend in the growth region before get transported to the electrode. At higher electric fields, NPs experience higher electric force and get quickly transported to the electrode, thus have comparatively smaller particle size.

2.2. HER Performance of Ni(OH)$_2$/NF Electrocatalysts

The electrocatalytic HER performance of different as-prepared Ni(OH)$_2$/NF electrocatalysts, without any post-processing, loading or adhesive coating treatments, were evaluated using three-electrode setup in an alkaline (1 M KOH) electrolyte medium.

Figure. 4a shows the linear sweep voltammetry (LSV) curves, with iR compensation, of different Ni(OH)$_2$/NF electrocatalysts along with the LSV curve of Pt rod and bare Ni foam as references.

It is clear from these curves that the Ni(OH)$_2$/NF@40 V electrocatalyst is the best HER performer with the highest current density at a given overpotential. For example: At an overpotential of 250 mV (see vertical dashed line in Figure 4a), the current density (69.5 mA/cm^2) for Ni(OH)$_2$/NF@40 V sample is about ~ 4 times higher than the Ni(OH)$_2$/NF@1 V (~ 17.5 mA/cm^2). The corresponding current density values are ~ 18.2 mA/cm^2, ~ 20.1 mA/cm^2, and ~ 24.9 mA/cm^2 for Ni(OH)$_2$/NF@5 V, Ni
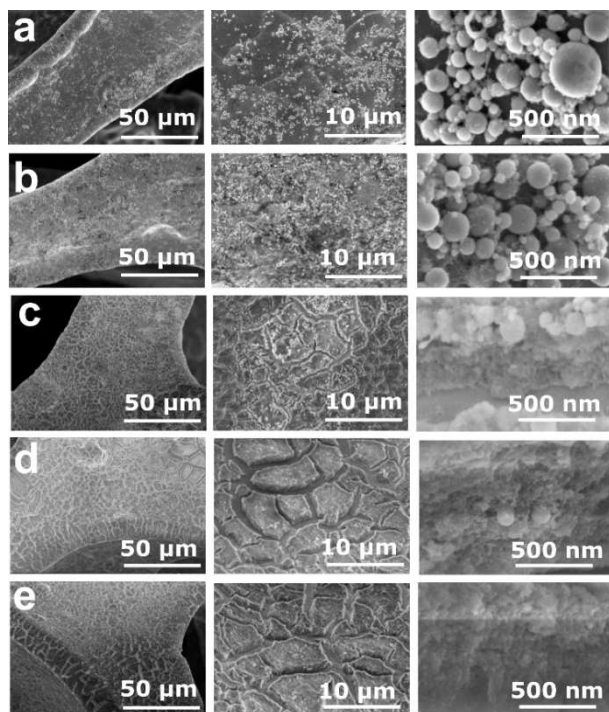
Figure 3. Surface morphological characterization of Ni/Ni(OH)2@NF NPs deposited on Ni foam: SEM images of Ni(OH)$_2$/NF electrocatalysts fabricated under a) 1, b) 5, c) 10, d) 25, and e) 40 V/cm of applied electric fields.
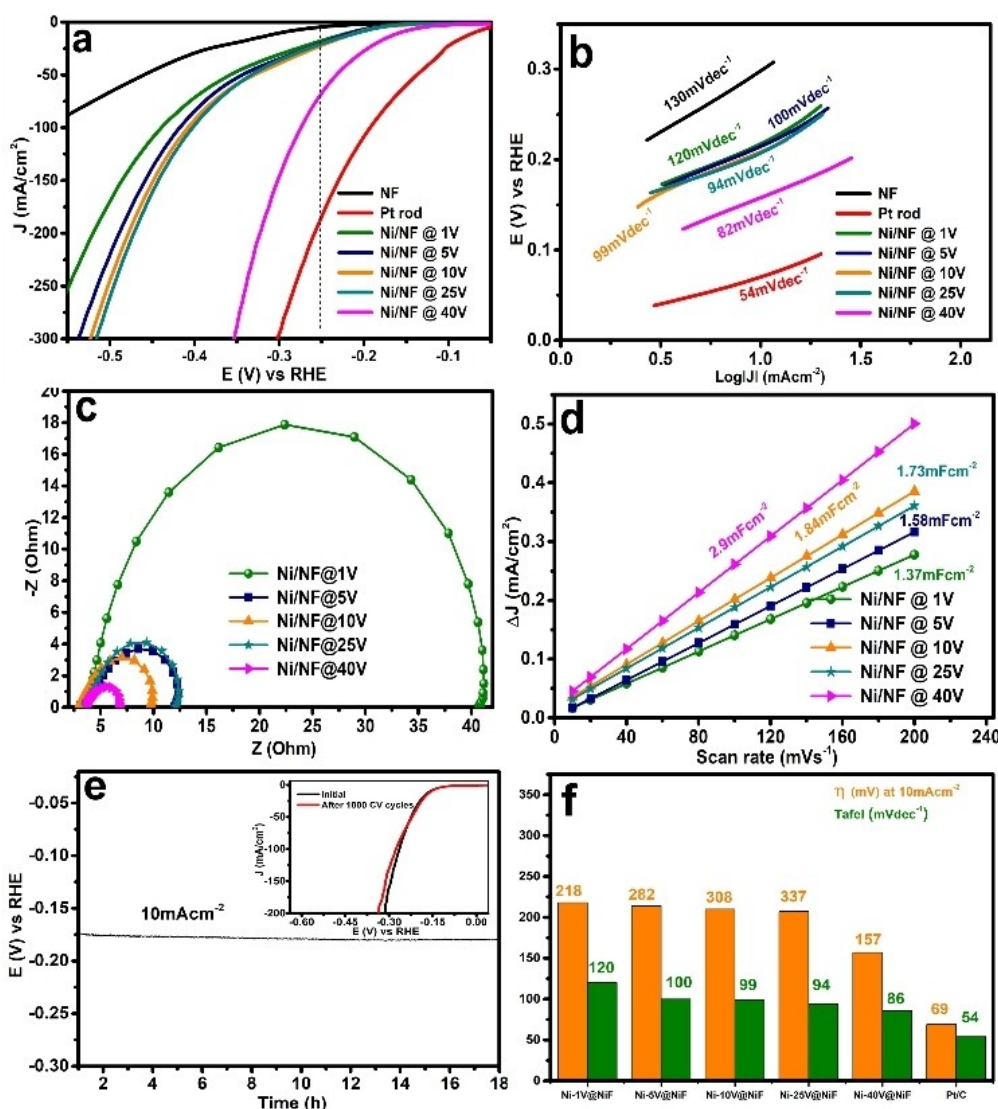
Figure 4. HER performance of Ni NPs electrophoretically deposited on Ni foam under different biased voltages and Pt/C electrode: a) polarization curves, b) corresponding Tafel slope, c) corresponding Nyquist plots. d) Estimation of double layer capacitance (C_{dl}) by plotting the mean of difference in cathodic and anodic currents with the scan rate. e) Chronopotentiometry test; inset: LSV curves before (solid black) and after (solid red 1000 CV cycles. f) Tafel slope and overpotentials (mV) for different samples.

$(OH)_2/NF$ @10 V, and $Ni(OH)_2/NF@25$ V electrocatalysts, respectively. The overpotential η_{10} value for the $Ni(OH)_2/NF@40$ V electrocatalyst is much lower (157 mV) as compared to the bare Ni foam (296 mV) and EF-PLA fabricated electrocatalysts produced at lower electric fields. For example: the η_{10} values for the $Ni(OH)_2/NF@1$ V, $Ni(OH)_2/NF@5$ V, $Ni(OH)_2/NF@10$ V, and $Ni(OH)_2/NF@25$ V electrocatalysts are 218, 214, 210, and 207 mV s, respectively. From the LSV measurements, we can say that the HER electrocatalyst fabricated under a higher applied electric field has higher HER performance. Similarly, the η_{200} (322 mV) and η_{100} (274 mV) overpotential values for $Ni(OH)_2/NF@40$ V electrocatalyst are higher than all other electrocatalysts produced at the lower electric fields.

As shown in Figure 4b, the calculated Tafel slopes for the samples bare Ni foam and $Ni(OH)_2/NF@1$ V, $Ni(OH)_2/NF@5$ V, Ni $(OH)_2/NF@10$ V, $Ni(OH)_2/NF$ @25 V, and $Ni(OH)_2/NF$ @40 V elec-

trocatalysts are ~130, 120, 100, 99, 94, and 82 mV/dec, respectively. The Tafel slopes and overpotential values for all the five EF-PLA produced electrocatalyst samples are summarized in Table 3 in the supporting information. The electrochemical impedance spectroscopy (EIS) (Figure 4c) of the electrocatalyst samples shows that $Ni(OH)_2/NF@40$ V (6.71 Ω) has significantly lower charge-transfer resistance as compared to $Ni(OH)_2/NF@25$ V (12.08 Ω), $Ni(OH)_2/NF@10$ V (9.67 Ω), Ni $(OH)_2/NF@5$ V (11.95 Ω), and $Ni(OH)_2/NF@1$ V (41.08 Ω) electrocatalysts resulting in a higher rate of electron transfer from the electrocatalyst for the reduction of surface adsorbed H* in the Volmer step of the HER. To further investigate the intrinsic activity of the electrocatalysts, we estimated the electrochemical active surface area (ECSA) using the corresponding double-layer capacitance (C_{dl}) value extracted from the CV curves recorded in the non-Faradaic region at different scan rates (see

ChemElectroChem

Articles
doi.org/10.1002/celc.202001511

Chemistry Europe
European Chemical
Societies Publishing

Figure S7). The Ni(OH)$_2$/NF@40 V exhibits the largest C$_{dl}$ value (2.9 mF/cm^2) as compared to Ni(OH)$_2$/NF@25 V (1.73 mF/cm^2), Ni(OH)$_2$/NF@10 V (1.84 mF/cm^2), Ni(OH)$_2$/NF@5 V (1.58 mF/cm^2), and Ni(OH)$_2$/NF@1 V (1.37 mF/cm^2) (Figure 4d) electrocatalysts. The corresponding C$_{dl}$ value (2.2 mF/cm^2) of the bare Ni foam is used to calculate ECSA values of different Ni(OH)$_2$/NF electrocatalysts (Supplementary information Table 3). It is interesting to see that the ECSA values of Ni(OH)$_2$/NF electrocatalysts fabricated under 1 to 25 V/cm of applied electric fields are higher (0.622 cm^2 for Ni(OH)$_2$/NF@1 V, 0.71 cm^2 for Ni(OH)$_2$/NF@5 V, 0.83 cm^2 for Ni(OH)$_2$/NF@5 V, and 0.78 cm^2 for Ni(OH)$_2$/NF@25 V) as compared to the bare Ni foam (1 cm^2). Enhancement in the HER performance of the EF-PLA produced Ni(OH)$_2$/NF electrocatalysts despite of the decrease in the corresponding ECSA values over the bare Ni foam indicates strong intrinsic HER activity of the laser produced NPs. The enhanced HER performance of the Ni(OH)$_2$/NF@40 V electrocatalyst (ECSA value; 1.32 cm^2) over the bare Ni foam is due to synergistic effect of enhanced ECSA value and large intrinsic activity of Ni(OH)$_2$ NPs.

Moreover, the long-term durability of an electrocatalyst is an important performance parameter to estimate its electrochemical performance. As can be seen from the chronopotentiometry curve in Figure 4e, nearly constant overpotential, a very small variation in the potential ($\Delta V \sim 4$ mV) is recorded after 18 hours, when Ni(OH)$_2$/NF@40 V sample is used as the working electrode. Additionally, the LSV curve of Ni(OH)$_2$/NF@40 V sample after 1000 CV cycles (inset Figure. 4e) has no obvious change from the corresponding initial CV curve. The results obtained from these investigations show an excellent electrochemical stability of the Ni(OH)$_2$/NF@40 V electrocatalyst in an alkaline electrolyte.

2.3. OER Performance of Ni(OH)$_2$@NF Electrocatalysts

The electrocatalytic OER performances of different as-prepared Ni(OH)$_2$/NF electrocatalysts were investigated in the same alkaline (1 M KOH) electrolyte medium. The OER LSV curves for different Ni(OH)$_2$/NF electrocatalysts along with bare Ni foam and RuO$_2$ powder are shown in Figure 5a. As can be seen from these LSV curves, the overpotential (η_{20}) is significantly lower for Ni(OH)$_2$/NF@40 V (184 mV) as compared to the bare Ni foam (530 mV), Ni(OH)$_2$/NF@1 V (440 mV), Ni(OH)$_2$NF@5 V (448 mV), Ni(OH)$_2$NF@10 V (430 mV), Ni(OH)$_2$/NF@25 V (420 mV), and RuO$_2$ (385 mV) electrocatalysts (inset Figure 6a). Similarly, the value of η_{50} is also minimum for Ni(OH)$_2$/NF@40 V (491 mV) as compared to Ni(OH)$_2$/NF@1 V (614 mV), Ni(OH)$_2$/NF@5 V (598 mV), Ni(OH)$_2$NF@10 V (569 mV), Ni(OH)$_2$/NF@25 V (539 mV) and RuO$_2$ (495 mV) electrocatalysts. As shown in Figure 5b, the calculated Tafel slopes for Ni(OH)$_2$/NF@40 V, Ni(OH)$_2$/NF@25 V, Ni(OH)$_2$/NF@10 V, Ni(OH)$_2$/NF@5 V, Ni(OH)$_2$/NF@1 V, bare Ni foam, and RuO$_2$ electrocatalysts are 74 mV/dec, 106 mV/dec, 93 mV/dec, 80 mV/dec, 146 mV/dec, and 63 mV/dec, respectively. The Tafel slopes and overpotential values for different Ni(OH)$_2$/NF electro-

catalysts are presented in Figure 5b and summarized in Table S4 in the Supporting Information.

The EIS of these samples shows that Ni(OH)$_2$/NF@40 V has significantly lower charge-transfer resistance as compared to Ni(OH)$_2$/NF electrocatalysts fabricated at a lower applied electric fields (Figure 5c) resulting in comparatively higher rate of charge transfer at the electrode-adsorbate interface for the oxidation of intermediates (OH*, OOH*, O*), adsorbed on the electrocatalyst surface, responsible for the OER. Figure 5c shows that the charge-transfer resistance of Ni(OH)$_2$/NF@40 V, Ni(OH)$_2$/NF@25 V, Ni(OH)$_2$/NF@10 V, Ni(OH)$_2$/NF@5 V, and Ni(OH)$_2$/NF@1 V electrocatalysts are 58.53 Ω, 102.01 Ω, 79.1 Ω, 260.9 Ω, and 2024.4 Ω, respectively. To further explore the intrinsic activity of different electrocatalysts against OER, we estimated their ECSA values using corresponding C$_{dl}$ values extracted from the CV curves recorded in the non-Faradaic region (1.37 to 1.39 V) at different scan rates (see Figure S8). The Ni(OH)$_2$/NF@40 V electrocatalyst exhibits significantly higher (the largest among all) C$_{dl}$ value (86.4 mF/cm^2) over Ni(OH)$_2$/NF@25 V (50 mF/cm^2) and Ni(OH)$_2$/NF@10 V (56 mF/cm^2), Ni(OH)$_2$/NF@5 V (39 mF/cm^2), and Ni(OH)$_2$/NF@1 V (23 mF/cm^2) and, the bare Ni foam (NF) 10.1 (see Figure 5d and Figure S8). The measured C$_{dl}$ values show significantly larger) ECSA values for EF-PLA fabricated electrocatalysts (~8.5 cm^2 for Ni(OH)$_2$/NF@40, ~4.9 cm^2 for Ni(OH)$_2$/NF@25 V, ~5.5 cm^2 for Ni(OH)$_2$/NF@10 V, ~3.8 cm^2 for Ni(OH)$_2$/NF@5 V, and ~2.3 cm^2 for Ni(OH)$_2$/NF@1 V) over the bare Ni foam (1 cm^2) substrate.

The long-term durability of Ni(OH)$_2$/NF@40 V sample, the best OER performer, was tested for 24 hours of chronopotentiometry (CP) curve at ~20 mA/cm^2 (Figure 5e). Very small change in (only ~0.6%) the potential in the course of 24 hours indicates excellent durability of the Ni(OH)$_2$/NF@40 V OER electrocatalyst in the alkaline medium. The corresponding LSV curves before and after 500 CV cycles (inset of Figure 5e) exhibit almost complete overlap of the two curves. A histogram with the η_{10} overpotential and Tafel slopes of different EF-PLA produced Ni(OH)$_2$/NF electrocatalysts and RuO$_2$ is shown in Figure 5f.

2.4. Water Splitting Performance of Ni(OH)$_2$@NF Electrocatalysts

Following the above mentioned HER and OER results, where Ni/NF@40 V electrocatalyst was the best HER and OER performer in the alkaline medium, we constructed a two-electrode electrochemical cell Ni(OH)$_2$/NF@40 V || Ni(OH)$_2$/NF@40 V electrocatalysts as the cathode and anode for overall water splitting in 1 M KOH electrolyte. Another two electrode cell (NF || NF) having bare Ni foams as cathode and anode was also fabricated for comparison.

The cell was connected to BioLogic VMP3 multichannel workstation with a two-electrode system. The linear sweep voltammetry curves for both electrochemical cells are shown in figure. 6a. It is evident from these curves that Ni(OH)$_2$/NF@40 V || Ni(OH)$_2$/NF@40 V cell has significantly higher current density at a given potential over the NF || NF cell. As can be
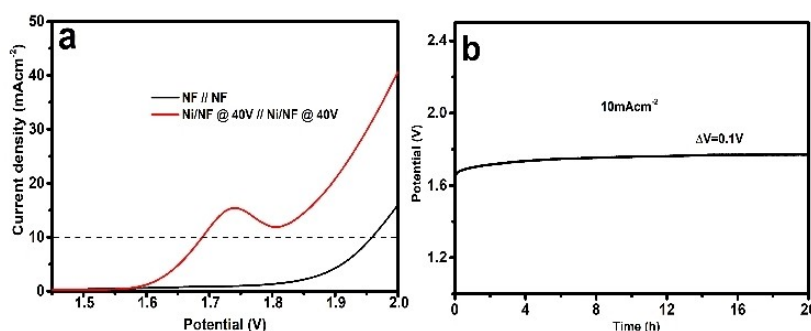
Figure 6. Overall water splitting performance for the electrochemical cell made of Ni/NF@ 40 V as cathode as well as anode in alkaline medium: a) polarization curve and b) long-term stability through chronoamperometry for 20 hours.
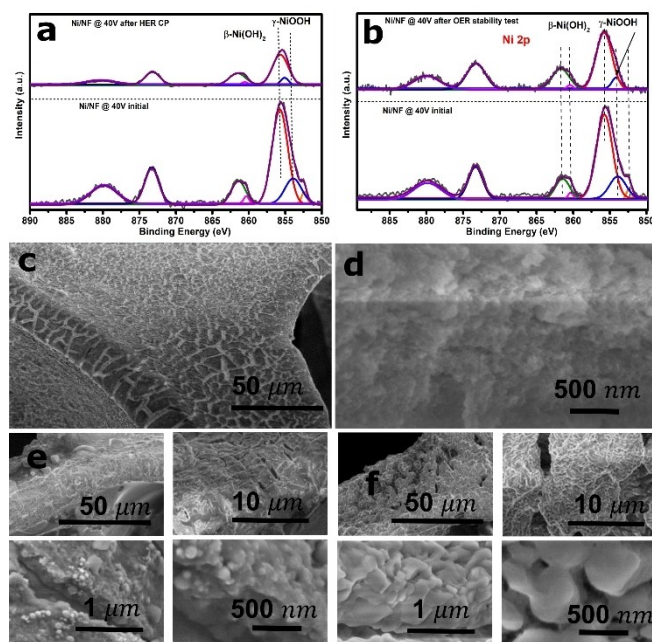
seen only 1.68 V overpotential is required to drive 10 mA/cm^2 of current density in Ni(OH)$_2$/NF@40 V | | Ni(OH)$_2$/NF@40 V cell, while the corresponding potential for NF | | NF cell is 1.96 V. This means that functionalization of NF electrode with EF-PLA produced NPs reduces the electric potential required to drive 10 mA/cm^2 current density by 280 mV. For the durability testing of the Ni(OH)$_2$/NF@40 V | | Ni(OH)$_2$/NF@40 V electrochemical cell, we employed chronopotentiometry at a constant current density of 10 mA cm^{-2} for 20 h. As can be seen from Figure 6b, the potential required to drive 10 mA/cm^2 of the current density is maintained for 20 h and only 0.1 V elevation in required potential is recorded, indicating an excellent durability of the HER and OER electrocatalysts for overall water splitting in the alkaline medium.

2.5. XPS after Electrochemical Measurements

The formation of nickel hydroxide as predicted by the pre-XRD and XPS was further confirmed by the post-treatment XPS analysis. After the HER and OER stability test, it was found that there is variation in the XPS spectrum obtained at different sites on the same sample. Representative spectra shown in Figure 7a and 7b for Ni 2p (for HER and OER respectively).

The Ni 2p$_{3/2}$ spectrum before the HER/OER measurements shows the emergence of an additional peak at 852.5 eV which can be ascribed to the Ni. (Figure 2 right column last panel). The observation of a peak in the O 1s spectrum at 529.4 eV also supports Ni(OH)$_2$ formation, (see Figure S9). Interestingly, after HER and OER stability tests, there was a slight shift to lower binding energy in the O 1s spectrum to 531.3 eV to 531.0 eV. In addition, the peak maximum for Ni 2p$_{3/2}$ also shifted to a higher binding energy from 855.55 eV to 855.69 eV after stability test, also there is no peak at 852.8 eV after stability test.

Figure 7c-f represent pre and post SEM micrographs of sample prepared at 40 V/cm before electrochemical measurements. The morphology of the electrocatalysts remains unchanged after 20 hours of electrochemical test showing structural integrity and stability of EF-PLA produced Ni(OH)$_2$/NF electrocatalysts.

3. Conclusions

In summary, a single step, fast and sustainable approach is developed for the fabrication ready-to-use bifunctional electrocatalysts for overall water splitting. Electric field assisted pulsed laser ablation in liquid for generation of nanoparticles with simultaneous transportation of the growing NPs from solution to the biased Ni foam substrate fabricated electrocatalyst substrate in few minutes. The intensity of applied electric field effectively modulates size, morphology, composition and hence water splitting performance of as produced electrocatalysts. The as-fabricated electrocatalyst is found highly efficient and stable in alkaline medium for HER and OER kinetics with remarkably low overpotential of 187 mV (vs. RHE for HER) and 1.66 V(vs. RHE for OER) to reach current density of 20 mA cm^{-2} with HER and OER Tafel slopes of 82 and 69 mV dec^{-1},

Figure 7. XPS and SEM analysis of Ni/NF @40 V before and after the electrochemical measurements. a) Before and after HER-CP test, b) before and after OER-CP test. SEM c, d) before and e) after HER; f) after OER CP test.

ChemElectroChem

Articles
doi.org/10.1002/celc.202001511

Chemistry Europe
European Chemical
Societies Publishing

respectively. The two-electrode electrochemical cell made of the bifunctional Ni(OH)$_2$/NF electrocatalyst requires overpotential as low as 1.68 V to drive 10 mA/cm^2 current density over a long period. These results reveal long-term stability and activity of the Ni(OH)$_2$/NF electrocatalyst towards overall water (OW) splitting. The superior morphological robustness, lowest overpotential amongst all the reported Ni(OH)$_2$ catalysts, lower Tafel, superior activity over RuO$_2$, good stability during both cycling and chronopotentiometry suggest that the activated Ni(OH)$_2$/NF by surface faceting is the first-rate HER/OER catalyst with lower overpotential for durable water splitting as an cathode/anode material in alkaline condition. The developed sustainable approach of electrocatalyst fabrication can be extended to a range of materials, beyond Ni(OH)$_2$/NF, to boost a range of chemical reactions, beyond water splitting.

Experimental Section

Materials

The Ni disc, 99.999%, (Advanced materials professional manufacture, China), absolute ethanol, and diethyl ether were purchased from Sinopharm Chemical Reagent Co., Ltd. Ni foam (thickness 1.5 mm, porosity ~98%) were used as received. Deionized (DI) water (resistivity: 18.3 MΩ) was used, as received, as medium for the laser ablation and preparation of aqueous electrolyte solution without further purification.

Fabrication of Ni(OH)$_2$@NF Electrocatalysts

The Ni(OH)$_2$@NF electrocatalysts were prepared using electric field assisted pulsed laser ablation (EF-PLA) of a Ni target in water. Pulsed laser ablation synthesis of Ni nanoparticles in combination simultaneous *in-situ* dielectrophoretic deposition of as-produced NPs on Ni foam were used to prepared Ni(OH)$_2$@NF electrocatalysts. Briefly, a Ni disc, placed at the bottom of glass vessel containing 1.5 cm thick layer of deionized water, was allowed to irradiate using a pulsed laser beam from Spectra Physics Spitfire Ti: Sapphire laser (wavelength(λ) 800 nm, pulse duration (τ) 200 ps, repetition rate: 1 kHz, and pulse energy 0.5 mJ/pulse). A 200 mm focal plano-convex lens was used to focus the laser beam normal to the target surface at the target-liquid interface through the transparent liquid overlayer. The water reservoir along with the target was mounted at the platform of a motorized X–Y translational stage and moved in the spiral fashion with the speed of 1 mm/s so that each laser pulse ablate a fresh surface. The electric field across the laser produced plasma and dielectrophoretic deposition was produced by dc biasing of a pair of parallel Ni-foam electrodes (size: 30 mm × 5 mm × 1 mm) with 1 cm separation. The electric field (1, 5, 10, 25, and 40 V/cm) was varied by varying the dc biasing voltage between the electrodes and maintaining their separation. Each sample was fabricated by ablation and dielectrophoretic deposition at Ni foam for 80 minutes.

Characterization of Electrocatalysts

The UV-visible absorption spectra of the ITO deposited NPs, from the ablation vessel during dielectrophoretic deposition, were measured in the spectral range of 200–800 nm using Cary 300 (Agilent Technologies) double beam spectrophotometer. The x-ray diffraction (XRD) measurements of as-prepared samples, Ito deposited via in situ di-electrodeposition, were carried out using Bruker D8 Focus X-ray diffractometer with Cu–Kα (λ = 1.5406 Å) radiation operating at a voltage of 40 kV and a current of 30 mA. The Raman spectra of samples, ITO deposited NPs, from the ablation vessel during dielectrophoretic deposition, were measured using a LabRAM HR Evolution Raman spectrometer (Horiba Jobin Yvon). The scanning electron microscopic (SEM) images of NiO/Ni(OH)$_2$@NF electrocatalysts, before and after electrochemical measurement, were measured using a HITACHI S4800 scanning electron microscope. The X-ray photoelectron spectra were recorded using Thermo Escalab 250XI X-ray photoelectron spectroscopy with AlKα X-ray source.

Electrochemical Measurements

The electrochemical measurements were performed on BioLogic VMP3 multichannel workstation with a three-electrode system, where a Ni foam, EF-PLA fabricated Ni(OH)$_2$@NF electrocatalyst (0.5 cm × 0.5 cm), and a saturated calomel electrode (SCE) were used as counter, working and reference electrodes, respectively. An aqueous solution of 1 M KOH was used as electrolyte in all the electrochemical measurements. Each of the working electrode was pre-scanned for 60 Cycles of cyclic voltammetry (CV) with the scan rate 40 mV s^{-1} before performing linear sweep voltammetry (LSV) curves. The LSV curves were measured by sweeping voltage in the range of −0.2 to −1.6 V vs SCE electrode with the scan rate of 10 mV s^{-1}. The expression $E_{RHE} = E_{SCE} + E^0_{SCE} + 0.0592 * pH$, where $E^0_{SCE} = 0.242$ V, was used to translate V *versus* SCE to V *versus* reverse hydrogen electrode (RHE). Electrochemical impedance spectroscopy (EIS) was measured at a dc overpotential of −0.34 V vs RHE (For HER) and +1.14 V vs RHE (for OER) and superimposing a small alternating voltage of 10 mV over the frequency range of 0.01 Hz to 1 MHz. The CV curves were further measured in the non-Faradaic region of potential from 0.84 V to 1.04 V (*versus* RHE) for HER and from 1.23 V to 1.54 V (*versus* RHE) for OER with different scan rates (from 10 mV s^{-1} to 120 mV s^{-1} for HER, and from 10 mV s^{-1} to 80 mV s^{-1} for OER) to estimate the double layer capacitance (C$_{dl}$) and electrochemically active surface area (ECSA). The slope of the difference in the cathodic and anodic current densities ($\Delta J = J_c − J_a$) with the scan rate resulted C$_{dl}$. The ECSA values were then calculated using the expression $ESCA_{Ni@NF} = C_{dl\,Ni@NF}/C_{dl-NF}$; where C$_{dl\,NF}$ is the double layer capacitance for the bare Ni foam. All the electrochemical measurements were performed at room temperature. The long-term durability measurements were done using 24 hours of chronopotentiometry (CP) and LSV curves before and after the CP measurements.

Conflict of Interest

The authors declare no conflict of interest.

[1] J. Lelieveld, K. Klingmüller, A. Pozzer, R. T. Burnett, A. Haines, V. Ramanathan, *Proc. Natl. Acad. Sci. USA* **2019**, *116*, 7192.
[2] H. McJeon, J. Edmonds, N. Bauer, L. Clarke, B. Fisher, B. P. Flannery, J. Hilaire, V. Krey, G. Marangoni, R. Mi, K. Riahi, H. Rogner, M. Tavoni, *Nature* **2014**, *514*, 482.
[3] D. Shindell, C. J. Smith, *Nature* **2019**, *573*, 408.
[4] J. Krane, *MRS Energy Sustainability* **2017**, *4*, 1.
[5] B. K. Sovacool, P. Schmid, A. Stirling, G. Walter, G. MacKerron, *Nat. Energy* **2020**.
[6] A. Kätelhön, R. Meys, S. Deutz, S. Suh, A. Bardow, *Proc. Natl. Acad. Sci. USA* **2019**, *166*, 11187.
[7] K. T. Møller, T. R. Jensen, E. Akiba, H. wen Li, *Prog. Nat. Sci.* **2017**, *27*, 34.
[8] I. Staffell, D. Scamman, A. Velazquez Abad, P. Balcombe, P. E. Dodds, P. Ekins, N. Shah, K. R. Ward, *Energy Environ. Sci.* **2019**, *12*, 463.
[9] S. Y. Tee, K. Y. Win, W. S. Teo, L. D. Koh, S. Liu, C. P. Teng, M. Y. Han, *Adv. Sci.* **2017**, *4*.
[10] T. Shinagawa, K. Takanabe, *ChemSusChem* **2017**, *10*, 1318.
[11] B. Lai, S. C. Singh, J. K. Bindra, C. S. Saraj, A. Shukla, T. P. Yadav, W. Wu, S. A. McGill, N. S. Dalal, A. Srivastava, C. Guo, *Mater. Today Commun.* **2019**, *14*.
[12] S. Guan, X. Fu, Z. Lao, C. Jin, Z. Peng, *Sustain. Energy Fuels* **2019**, *3*, 2056.
[13] X. Zheng, X. Han, Y. Zhang, J. Wang, C. Zhong, Y. Deng, W. Hu, *Nanoscale* **2019**, *11*, 5646.
[14] J. Zhang, Y. Wang, C. Zhang, H. Gao, L. Lv, L. Han, Z. Zhang, *ACS Sustainable Chem. Eng.* **2018**, *6*, 2231.
[15] A. L. Wang, H. Xu, G. R. Li, *ACS Energy Lett.* **2016**, *1*, 445.
[16] S. Li, C. Xi, Y. Z. Jin, D. Wu, J. Q. Wang, T. Liu, H. Bin Wang, C. K. Dong, H. Liu, S. A. Kulinich, X. W. Du, *ACS Energy Lett.* **2019**, *4*, 1823.
[17] L. Chen, X. Dong, Y. Wang, Y. Xia, *Nat. Commun.* **2016**, *7*, 1.
[18] Q. Zhang, C. Zhang, J. Liang, P. Yin, Y. Tian, *ACS Sustainable Chem. Eng.* **2017**, *5*, 3808.
[19] D. Wang, Q. Li, C. Han, Z. Xing, X. Yang, *ACS Cent. Sci.* **2018**, *4*, 112.
[20] P. C. Ray, H. Yu, P. P. Fu, Toxicity and environmental risks of nano-materials: Challenges and future needs; **2009**; Vol. 27.
[21] V. Misra, S. D. Pandey, *Environ. Int.* **2005**, *31*, 417.
[22] I. Hussain, N. B. Singh, A. Singh, H. Singh, S. C. Singh, *Biotechnol. Lett.* **2016**, *38*, 545.
[23] Y. Rho, J. Pei, L. Wang, Z. Su, M. Eliceiri, C. P. Grigoropoulos, *ACS Appl. Mater. Interfaces* **2019**, *11*, 39385.
[24] T. Zou, B. Zhao, W. Xin, Y. Wang, B. Wang, X. Zheng, H. Xie, Z. Zhang, J. Yang, C. Guo, *Light: Sci. Appl.* **2020**, *9*, 1.
[25] A. Y. Vorobyev, C. Guo, *Laser Photonics Rev.* **2013**, *7*, 385.
[26] Z. Zhan, M. Elkabbash, J. L. Cheng, J. Zhang, S. Singh, C. Guo, *ACS Appl. Mater. Interfaces* **2019**, *11*, 48512.
[27] S. C. Singh, M. ElKabbash, Z. Li, X. Li, B. Regmi, M. Madsen, S. A. Jalil, Z. Zhan, J. Zhang, C. Guo, *Nature Sustainability* **2020**, *3*, 938.
[28] R. K. Swarnkar, S. C. Singh, R. Gopal, *AIP Conf. Proc.* **2009**, *1147*, 205.
[29] H. Zeng, X. W. Du, S. C. Singh, S. A. Kulinich, S. Yang, J. He, W. Cai, *Adv. Funct. Mater.* **2012**, *22*, 1333.
[30] S. C. Singh, R. Gopal, *J. Nanoeng. Nanomanuf.* **2013**, *3*, 365.
[31] Z. Li, Y. Zhang, Y. Feng, C. Q. Cheng, K. W. Qiu, C. K. Dong, H. Liu, X. W. Du, *Adv. Funct. Mater.* **2019**, *29*.
[32] P. Wagener, A. Schwenke, S. Barcikowski, *Langmuir* **2012**, *28*, 6132.
[33] F. Lin, J. Yang, S. H. Lu, K. Y. Niu, Y. Liu, J. Sun, X. W. Du, *J. Mater. Chem.* **2010**, *20*, 1103.
[34] M. Ikeda, Y. Kusumoto, H. Yang, S. Somekawa, M. Uenjyo, M. Abdulla-Al-Mamun, Y. Horie, *Catal. Commun.* **2008**, *9*, 1329.
[35] A. P. Grosvenor, M. C. Biesinger, R. S. C. Smart, N. S. McIntyre, *Surf. Sci.* **2006**, *600*, 1771.
[36] M. C. Biesinger, B. P. Payne, L. W. M. Lau, A. Gerson, R. S. C. Smart, *Surf. Interface Anal.* **2009**, *41*, 324.